Science Bulletin 64 (2019) 823–835

Contents lists available at ScienceDirect

Science Bulletin

journal homepage: www.elsevier.com/locate/scib

Article

High-performance meta-devices based on multilayer meta-atoms: interplay between the number of layers and phase coverage

Bowen Yang [a,1], Tong Liu [b,1], Huijie Guo [b], Shiyi Xiao [a,c,*], Lei Zhou [b,*]

[a] Key Laboratory of Specialty Fiber Optics and Optical Access Networks, Joint International Research Laboratory of Specialty Fiber Optics and Advanced Communication, Shanghai University, Shanghai 200444, China
[b] State Key Laboratory of Surface Physics, Key Laboratory of Micro and Nano Photonic Structures, Physics Department, Fudan University, Shanghai 200433, China
[c] Shanghai Institute for Advanced Communication and Data Science, Shanghai University, Shanghai 200444, China

ARTICLE INFO

Article history:
Received 21 March 2019
Received in revised form 4 May 2019
Accepted 27 May 2019
Available online 5 June 2019

Keywords:
Metasurface
Transparent window
Wave plate
Beam deflector

ABSTRACT

Transmissive metasurfaces have provided an efficient platform to manipulate electromagnetic (EM) waves, but previously adopted multilayer meta-atoms are too thick and/or the design approach fully relies on brute-force simulations without physical understandings. Here, based on coupled-mode theory (CMT) analyses on multilayer meta-atoms of distinct types, it is found that meta-atoms of a specific type only allows the phase coverage over a particular range, thus suitable for polarization-control applications. However, combinations of meta-atoms with distinct types are necessary for building ultra-thin wavefront-control meta-devices requiring 360° phase coverage. Based on these physical understandings, high-efficiency meta-atoms are designed/fabricated, and used to construct three typical meta-devices, including quarter- and half-wave plates and a beam deflector. Our results elucidate the physics underlying the interplay between thicknesses and performances of transmissive metasurfaces, which can guide the realizations of miniaturized transmissive meta-devices in different frequency domains.

1. Introduction

Metasurfaces refer to the ultra-thin metamaterials constructed by subwavelength planar microstructures (e.g., "meta-atoms"), which exhibit tailored electromagnetic (EM) properties. They have drawn intensive attention recently [1–4]. Through carefully adjusting the structures of the "meta-atoms", one can realize metasurfaces to exhibit desired distributions of phase and amplitude for reflected/transmitted waves. They can be used to efficiently reshape the wavefronts of incident EM waves based on Huygens-Fermat's principle. Many fascinating wave-manipulation effects have been realized based on metasurfaces, such as anomalous reflection and refraction [5,6], vortex beam generation [5,7], surface wave coupling [8], and giant and flexible spin-Hall effect [9,10]. Such extraordinary wave-manipulation capabilities inspire researchers to realize many functional metasurface-based optical devices such as flat lenses [11–14], ultrathin wave plates [15,16], and beam deflectors [17–19].

Among these applications, thickness and performance are two critical issues that must be considered simultaneously during the design of a meta-device. Ideally, ultra-thin meta-devices with high performances (e.g., high efficiency and broad bandwidth) are needed; but in reality thickness and performance affect each other due to the subtle interplay between them. To build a high-performance meta-device, a series of meta-atoms exhibiting nearly 100% transmission/reflection amplitudes with phases covering the full 360° range are required. For reflection-type metasurfaces, metal-insulator-metal (MIM) meta-atoms can fulfill these requirements, which hence have been widely used to build functional meta-devices with ultrathin thicknesses and high performances [8,12,20–24]. However, for transmission geometry, ultra-thin transparent meta-atoms with full-range phase coverage are quite difficult to obtain [25]. In order to make a meta-atom optically transparent, it must simultaneously exhibit electric and magnetic responses so that its impedance can match that of air [4]. In 2013, Pfeiffer and Grbic [17] realized the first transmissive metasurface (usually called Huygens' surfaces) based on a series of composite meta-atoms combining carefully designed electric resonators and magnetic split-ring-resonators. Based on a similar concept, researchers also proposed all-dielectric metasurfaces that were consisted of dielectric meta-atoms possessing spectrally overlapping electric and magnetic resonances with equal strengths [26]. Although such an idea was proven useful in designing high-efficiency transmissive meta-devices [18,27,28], the adopted meta-atoms usually involve complex three-dimensional (3D)

SPECIAL TOPIC: Electromagnetic Metasurfaces: from Concept to Applications.

* Corresponding authors.
E-mail addresses: phxiao@shu.edu.cn (S. Xiao), phzhou@fudan.edu.cn (L. Zhou).

[1] These authors contributed equally to this work.

https://doi.org/10.1016/j.scib.2019.05.028
2095-9273/

structures, which are optically thick and non-flat, and thus unfavorable for practical applications. To address this issue, multilayer meta-atoms were widely used to build transmissive metasurfaces at frequencies ranging from microwave to infrared [18,19,29]. In these meta-devices, the adopted meta-atoms all exhibit broadband transparent windows covering large phase-variation ranges (inset of Fig. 1), which enable researchers to select appropriate meta-atoms with desired transmission phases. Such meta-atoms are flat and easy to fabricate, and are widely used to realize functional meta-devices for different purposes [30–35].

However, despite this impressive progress, several fundamental issues remain unsolved. For example, having seen so many meta-devices with different layers, naturally, scientists are curious to know the minimum layer number and thickness required to build high-performance transmissive meta-devices. Several prior works [2,19,36,37] pointed out the phase coverage for meta-atoms with different layers. Unfortunately, unknowing the inherent physics underlying the intriguing interplay between the number of layers and performance, people usually have to employ brutal-force simulations to search for appropriate meta-atoms. It is not only time consuming, but also lacks physical guidance.

The main purpose of this work is to answer this fundamental question and to provide useful guidance for the practical design of transmissive metasurfaces. To achieve this goal, first coupled-mode-theory (CMT) analyses are performed to reveal the subtle interplays between thickness and phase-variation in multilayer meta-atoms of distinct types. It is found that meta-atoms with a particular type can provide transmission phases covering only a particular range (Fig. 1b–d). Therefore, combinations of meta-atoms with distinct types are highly suggested when building ultra-thin wavefront-control meta-devices that require full-range phase coverage. Based on these physical understandings, three meta-devices exhibiting distinct functionalities are designed and/or fabricated, which are a quarter wave plate (QWP), a half wave plate (HWP) and a beam deflector. Our findings are helpful for realizing transmissive meta-devices with both ultra-thin thicknesses and high performances in different frequency regimes.

2. CMT analyses on meta-atoms with different numbers of resonators

We start from analyzing the generic EM responses of two distinct types of meta-atoms, widely used in building transmissive meta-devices [25,32,34,35,38–41]. In the first type, the meta-atoms contain different layers of planar resonators (metallic crosses). Each is embedded inside a subwavelength metallic mesh, which is optically opaque below around working frequencies (Fig. 1b, c). In the second type, the only difference is that there is no metallic mesh surrounding the resonators. Here, the metallic mesh processes a cutoff frequency (much higher than the working frequency of the device), below which EM waves are strongly reflected. Thus, the metallic mesh serves as an optically opaque background for the whole system. Firstly, a 2-layer meta-atom of the first type is studied, which is described by a 2-port 2-mode model consisting of two coupled resonators (i.e., the loaded resonating structures) embedded in an opaque background (i.e., the mesh), as shown in Fig. 1b. Due to the presence of the opaque background, these two resonators can only be excited by external light coming from one particular port; also they can only radiate to that port. Meanwhile, these two resonators can couple with each other through near-field coupling with a strength of κ. Therefore, according to the tight binding method (TBM) established for photonic systems [42], the time-evolution of the two modes' amplitudes (denoted as a_1 and a_2) can be expressed as

$$\frac{1}{2\pi}\frac{\mathrm{d}}{\mathrm{d}t}\begin{pmatrix}a_1\\a_2\end{pmatrix}=\mathrm{i}\hat{\mathbf{H}}\begin{pmatrix}a_1\\a_2\end{pmatrix}=\mathrm{i}\begin{pmatrix}f_0&\kappa\\\kappa&f_0\end{pmatrix}\begin{pmatrix}a_1\\a_2\end{pmatrix}, \tag{1}$$

where f_0 denotes the resonant frequency of the mode supported by a single resonator. Here, assume the neighboring resonators are weakly coupled (i.e., $|\kappa|\ll f_0$) to satisfy the assumption of TBM. In Eq. (1), we have purposely "turned off" the mode's radiations to the far field at the moment, in order to see clearly the dynamical evolutions of the "modes" [43,44]. Diagonalizing the Hamiltonian matrix with a matrix $M=\frac{1}{\sqrt{2}}\begin{pmatrix}-1&1\\1&1\end{pmatrix}$, we obtain

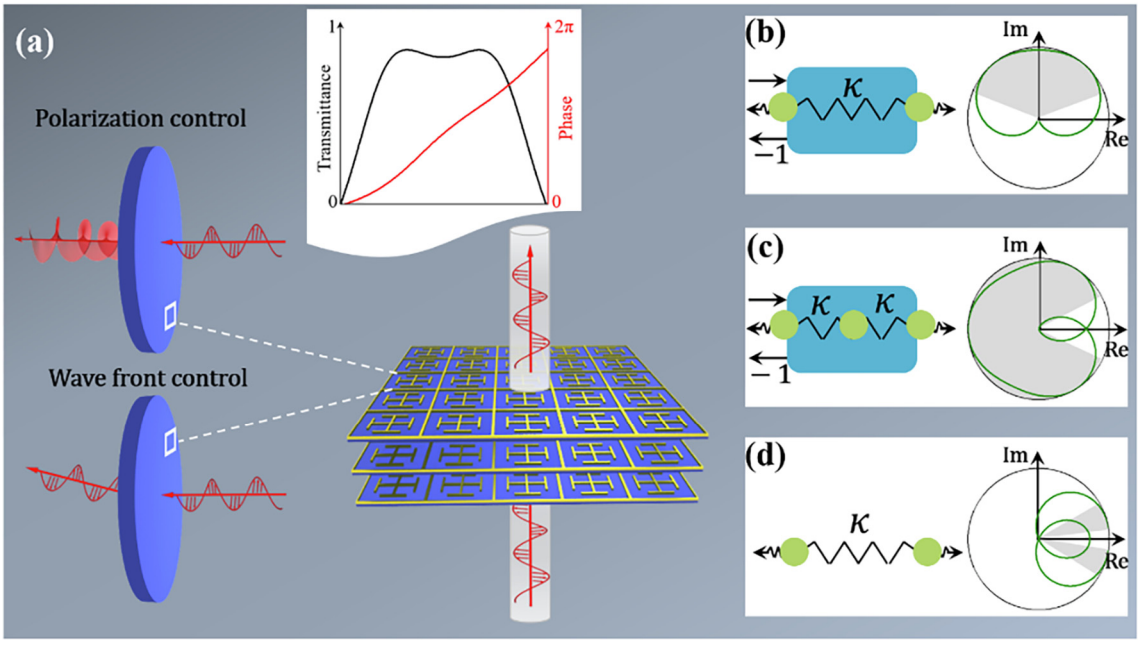

Fig. 1. Illustration of the transparent meta-atoms. (a) Schematics of transmissive meta-atoms for realizing polarization-control and beam deflecting meta-devices; Smith diagrams and phase coverage achieved by coupled-mode models with (b) two and (c) three resonators embedded in opaque background, and a coupled-mode model with (d) two resonators in a transparent background.

$$M \cdot \begin{pmatrix} f_0 & \kappa \\ \kappa & f_0 \end{pmatrix} \cdot M^{-1} = \begin{pmatrix} f_s & 0 \\ 0 & f_a \end{pmatrix}, \tag{2}$$

where the frequencies and wave-functions of two eigen collective modes are

$$\begin{cases} f_s = f_0 + \kappa, & |\psi_s\rangle = (|\varphi_1\rangle + |\varphi_2\rangle)/\sqrt{2}, \\ f_a = f_0 - \kappa, & |\psi_a\rangle = (|\varphi_1\rangle - |\varphi_2\rangle)/\sqrt{2}, \end{cases} \tag{3}$$

with $|\varphi_1\rangle$ and $|\varphi_2\rangle$ being the wave-functions of two original (uncoupled) resonators respectively. Here, "s" and "a" denote the symmetric and anti-symmetric natures of the two eigen collective modes correspondingly. Turning on the radiation channels of the modes, it is found through the CMT analyses [45] that the (complex) transmission coefficient t of the whole system (without considering material losses) can be expressed as

$$t = \frac{\Gamma_s}{-\mathrm{i}(f - f_s) + \Gamma_s} - \frac{\Gamma_a}{-\mathrm{i}(f - f_a) + \Gamma_a}, \tag{4}$$

where $\Gamma_s = \sum_i \left(|\langle k_i|\varphi_{1i}\rangle + \langle k_i|\varphi_{2i}\rangle|^2\right)/2$ and $\Gamma_a = \sum_i (|\langle k_i|\varphi_{1i}\rangle - \langle k_i|\varphi_{2i}\rangle|^2)/2$ denote the radiation damping rates of two collective modes towards two ports ($i = 1$ and 2), respectively. The parameters f_s, f_a, Γ_0 (or f_0, κ, Γ_0, equivalently) can in principle be calculated by direct integrations between wave-functions and external scattering waves. Here, for simplicity, we treat them as fitting parameters, which are retrieved by fitting the CMT curves with their simulation counterparts. The opaque background blocks the radiations of the resonator to one of the available ports; thus $\langle k_2|\varphi_1\rangle = \langle k_1|\varphi_2\rangle = 0$. Further considering the mirror symmetry possessed by the system, it is found that the radiation damping rates of two collective modes are identical ($\Gamma_s = \Gamma_a = \Gamma_0$). The second term in Eq. (4) exhibits a negative sign, caused by the antisymmetric nature of the second collective mode. Later we will show that this factor plays a much important role in enlarging the phase variation range of such a system.

Solid lines in Fig. 2a, b are the CMT-computed spectra with parameters $\kappa/f_0 = -0.2$, $\Gamma_0/f_0 = 0.15$ (both the near field coupling and the radiation damping rate are normalized by f_0). To further reveal the underlying physics, Fig. 2c depicts the transmission spectra calculated by two independent-oscillator models, i.e., $t_s = \Gamma_0/(-\mathrm{i}(f - f_s) + \Gamma_0)$ and $t_a = -\Gamma_0/(-\mathrm{i}(f - f_a) + \Gamma_0)$, as red and blue lines, respectively. Compared to the CMT-calculated transmission spectrum, though t_s and t_a can approximately describe the transmission spectrum at the immediate vicinities of two peaks, significant deviations exist in frequencies away from these two peaks. This is quite understandable since the final transmission spectrum is dictated by $t = t_s + t_a$ rather than t_s or t_a alone.

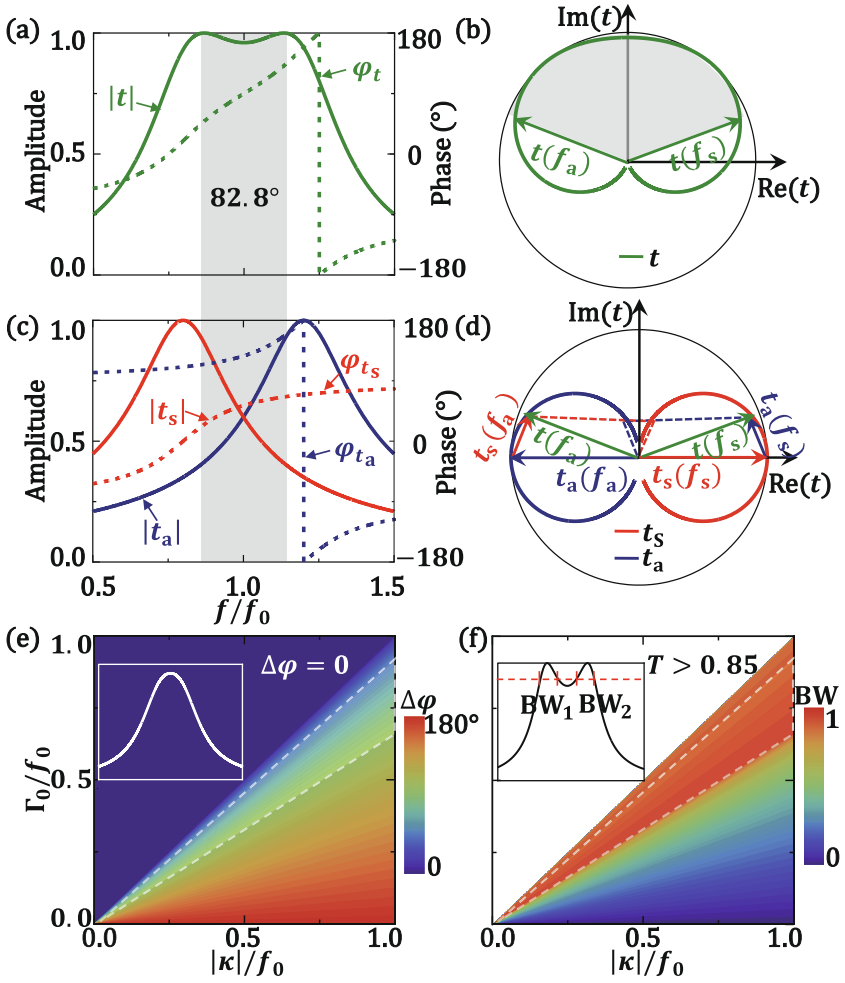

Fig. 2. Phase coverage for a 2-mode 2-port model in an opaque background. (a) CMT-computed spectra of transmission amplitude (solid line) phase (dashed line), and (b) Smith curve obtained for a 2-mode 2-port model in the opaque background with parameters $\kappa/f_0 = -0.2$, $\Gamma_0/f_0 = 0.15$. (c) The transmission amplitude (solid line), phase (dashed line), and (d) Smith curves of the anti-symmetric mode t_a (blue) and symmetric t_s mode. Phase diagrams of (e) phase coverage $\Delta\varphi$ and (f) transparency bandwidth Δf_{BW} versus Γ_0/f_0 and κ/f_0 calculated with CMT for the 2-mode-2-port model. Inset of (e) depicts the typical one-peak transmission spectrum within the weak-coupling region, and inset of (f) shows how transparency bandwidth Δf_{BW} is defined and calculated.

Hence, the interferences between the two modes are not negligible. In fact, the validities of two independent oscillators can only be justified when the considered two modes exhibit extremely large quality (Q) factors, which are highly undesired in meta-atom designs requiring flat transparency windows.

Such mode-interference effect can help us understand the phase variation inside the transparency window. Smith curves of t_s and t_a are separately depicted as blue and red lines in Fig. 2d, which represent two independent circles covering half space of the whole polar region without mutual interferences. Obviously, ignoring the mode interference effect, ideally, the transmission phase must vary from 0 to 180°, which covers a range of 180° as the frequency changes from f_s to f_a. However, in reality, the Smith curve of t (Fig. 2b) deviates significantly from that shown in Fig. 2d. In particular, now the two peak frequencies (f_s and f_a) do not locate exactly at the real axis (Fig. 2b); also the Smith curve does not touch the origin at a frequency in between the two peaks, both caused by the mutual interference between the two modes. As a result, the phase variation range inside the transparency window is only 82.8° (see the shaded region in Fig. 2a), less than 180° as predicted by Fig. 2d without considering the mode-interference effect.

Based on the above analyses, how to control the phase variation range in such 2-mode systems is discussed. Obviously, the mode-interference effects have close relations with the Q factors of two collective modes, which are in turn, dictated by the coupling strength κ and the radiation damping Γ_0 of the original mode. To quantify these arguments, CMT is used to compute the phase coverage $\Delta\varphi$ enabled by such two-mode systems as varying two model parameters Γ_0 and κ. Fig. 2e depicts the value $\Delta\varphi$ (color map) as a function of Γ_0 and κ. It is interesting to note that the line $\kappa = \Gamma_0$ separates the whole space into two sub-regions: the right-lower region with $0 < \Delta\varphi < 180°$ and the left-upper region with $\Delta\varphi = 0$. The physics is described in the following. Whereas the two resonators are coupled tightly yielding two well-defined transmission peaks in the strong-coupling ($\kappa > \Gamma_0$) region, no well-defined "modes" can be formed in the weak coupling ($\kappa < \Gamma_0$) region (see corresponding insets in Fig. 2e), where the rate of the radiation decay is higher than that of the inter-mode exchange. It is quite expectable that $\Delta\varphi$ covers a wide range in the strong-coupling region, but drops to zero in the weak-coupling region where no perfect transmission peak can be clearly identified.

In addition to the phase variation range $\Delta\varphi$, it is also essential to consider the amplitude fluctuations within the transparency band, for the purpose of practical meta-atom designs. To quantitatively measure such amplitude fluctuations, we define $\Delta f_{BW} = (BW_1 + BW_2)/2\kappa$ as the transparency bandwidth (see inset of Fig. 2f), which corresponds to the frequency region with high transmittance ($T > 0.85$). Fig. 2f depicts how Δf_{BW} varies against κ and Γ_0, which reveals a clear trade-off between $\Delta\varphi$ and Δf_{BW}. Whereas the available phase coverage $\Delta\varphi$ is maximized (approaching to 180°) at the limit of $\kappa \gg \Gamma_0$ (Fig. 2e), the transparency bandwidth Δf_{BW} approaches to zero in that limit. Instead, a large bandwidth is found in the region around $\kappa \sim 1.4\Gamma_0$, defined as "intermediate region" (shaded region in Fig. 2e, f), where the phase variation is only 90°, about half of the maximum phase coverage. Such intriguing trade-off between phase coverage and transparency bandwidth makes the 2-mode systems unsuitable for designing high-efficiency meta-devices with the purposes of wavefront-control, since these devices require full-range (360°) phase coverage coinciding with high transmission amplitudes. Instead, balancing the contradictory requirements on $\Delta\varphi$ and Δf_{BW}, it is found that such systems in the intermediate region are particularly suitable for designing high-performance polarization-control devices that do not need large phase coverage, such as quarter wave-plates.

After the intrinsic limitations of the 2-mode systems with an opaque background in providing wide-range phase coverage are understood, the possible strategies to solve the issue will be discussed. Obviously, adding more modes to the system is one possible solution. Still assuming that the background is opaque, CMT is used to analyze a 3-mode model (see Fig. 1c), obtained by adding another identical layer. First TBM [42] is used to obtain all collective modes. The Hamiltonian matrix can be written as

$$\frac{1}{2\pi}\frac{\mathrm{d}}{\mathrm{d}t}\begin{pmatrix} a_1 \\ a_2 \\ a_3 \end{pmatrix} = \mathrm{i}\hat{\mathbf{H}}\begin{pmatrix} a_1 \\ a_2 \\ a_3 \end{pmatrix} = \mathrm{i}\begin{pmatrix} f_0 & \kappa & 0 \\ \kappa & f_0 & \kappa \\ 0 & \kappa & f_0 \end{pmatrix}\begin{pmatrix} a_1 \\ a_2 \\ a_3 \end{pmatrix}. \tag{5}$$

Diagonalizing this Hamiltonian matrix, we obtain three eigen collective modes as

$$\begin{cases} f_1 = f_0 + \sqrt{2}\kappa, & |\Psi_1\rangle = \left(|\varphi_1\rangle + \sqrt{2}|\varphi_2\rangle + |\varphi_3\rangle\right)/2, \\ f_2 = f_0, & |\Psi_2\rangle = \left(|\varphi_1\rangle - |\varphi_3\rangle\right)/\sqrt{2}, \\ f_3 = f_0 - \sqrt{2}\kappa, & |\Psi_3\rangle = \left(|\varphi_1\rangle - \sqrt{2}|\varphi_2\rangle + |\varphi_3\rangle\right)/2. \end{cases} \tag{6}$$

Now turn-on the radiation channels and perform the CMT analyses [45] following the same processes as in the 2-mode system, then we get the transmission coefficient as

$$t = \frac{\Gamma_0}{\mathrm{i}(f - f_0) - \Gamma_0} - \frac{\Gamma_0(f - f_0)}{\mathrm{i}\left(f - f_0 - \sqrt{2}\kappa\right)\left(f - f_0 + \sqrt{2}\kappa\right) - \Gamma_0(f - f_0)}. \tag{7}$$

Fig. 3a and b depict the CMT-computed transmission spectra of a 3-mode system with $\kappa/f_0 = -0.2, \Gamma_0/f_0 = 0.04$. Three perfect transmission peaks are found in the transmission spectrum, which correspond to three collective modes with the resonance frequency f_1, f_2, and f_3, respectively. Neglecting far-field interactions (valid at the limit of $\Gamma_0 \ll \kappa$), the transmission amplitude can be expressed as $t \sim t_1 + t_2 + t_3$, where

$$\begin{cases} t_1 = \frac{\Gamma_0}{\mathrm{i}(f - f_0 - \sqrt{2}\kappa) + \Gamma_0}, \\ t_2 = \frac{\Gamma_0}{\mathrm{i}(f - f_0) + \Gamma_0}, \\ t_3 = \frac{\Gamma_0}{\mathrm{i}(f - f_0 + \sqrt{2}\kappa) + \Gamma_0}, \end{cases} \tag{8}$$

to represent the transmission coefficients of three independent oscillators. Considering the symmetries of these modes, one may easily find that at three (bare) resonant frequencies, t_1, t_2 and t_3 exhibit phases 0, 180°, 360°, respectively (see Fig. 3c). Therefore, ideally, if the mutual interferences between the three modes are completely neglected, the phase of t can cover up to 360°. However, in practice, mode-interference inevitably affects the phase coverage of the entire system, with the same physics as in the 2-mode system. As shown in Fig. 3d, mode-interference shifts the first and third peaks anticlockwise and clockwise, respectively; but the second peak is unaffected due to the symmetry protection, resulting in a smaller phase-variation range centered at 180°, as shown in Fig. 3b.

Fig. 3e depicts how $\Delta\varphi$ depends on κ and Γ_0, obtained by analyzing Eq. (7) in the similar way as in the 2-mode case. Similarly, it is found that a line $\left(\Gamma_0 = \sqrt{2}\kappa\right)$ separates the whole space into two regions, i.e., the weak-coupling region $\left(\sqrt{2}\kappa < \Gamma_0\right)$ where the transmission spectrum contains only one peak (inset of Fig. 3c), and the strong-coupling region ($\sqrt{2}\kappa \gg \Gamma_0$) with a relatively large phase-coverage range. However, Fig. 3f presents that the transparent bandwidth Δf_{BW} tends to become zero at the strong-coupling limit ($\sqrt{2}\kappa \gg \Gamma_0$), caused by the exceptionally high Q factors of

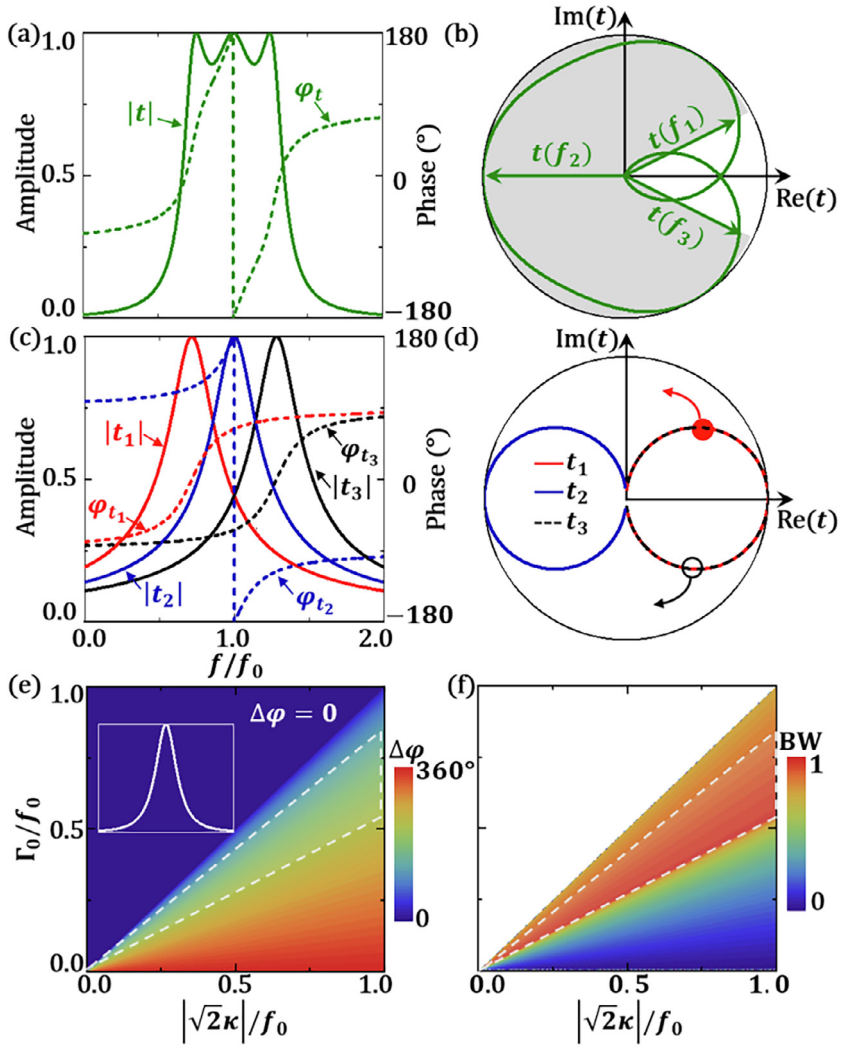

Fig. 3. Phase coverage for a 3-mode 2-port model in an opaque background. (a) CMT-computed spectra of transmission amplitude (solid line), phase (dashed line) and (b) Smith curve obtained for a 3-mode 2-port model in the opaque background with parameters $\kappa/f_0 = -0.2$, $\Gamma_0/f_0 = 0.04$. (c) The transmission amplitude (solid line), phase (dashed line), and (d) Smith cturves of three collective modes t_1 (red), t_2(blue) and t_3 (black) calculated by Eq. (8). Phase diagrams of (e) the phase coverage $\Delta\varphi$ and (f) transparency bandwidth versus Γ_0/f_0 and κ/f_0 calculated with CMT for 2-port 3-mode model. Inset of (e) depicts the typical single-peak transmission spectrum within the weak coupling region.

the transmission peaks. Balancing these two effects, it is found that the largest phase coverage that a 3-mode system (with an opaque background) can open is roughly 240° inside the intermediate region (i.e., with transmittance higher than 0.85).

After the key EM properties of the first type of meta-atoms (e.g., Fig. 1b, c) are learned, the second type of multilayer meta-atoms is studied, which can be described by CMT in a transparent background, as shown in Fig. 1d. Such meta-atoms have also been much widely used in building transmissive meta-devices [46,47]. Due to the differences in background properties, such model exhibits completely different EM properties (particularly the phase coverage properties) from its opaque-background counterpart, and therefore it may provide appropriate phases that cannot be covered by the opaque-background models. Specifically, the transmission coefficient of the 2-mode CMT (in a transparent background) is given by (see Supplementary Information Section I for mathematical derivation)

$$t = 1 + \frac{4\Gamma_0 \sin^2(\eta)}{\mathrm{i}(f - f_0 + \kappa) - 4\Gamma_0 \sin^2(\eta)} + \frac{4\Gamma_0 \cos^2(\eta)}{\mathrm{i}(f - f_0 - \kappa) - 4\Gamma_0 \cos^2(\eta)}, \quad (9)$$

where η represents the phase difference of two resonators' radiations toward forward and backward directions, closely related to the distance between two resonators. Solid lines in Fig. 4a, b are the CMT-computed spectra with parameters $\kappa/f_0 = -0.2$, $\Gamma_0/f_0 = 0.04$ and $\eta = 0.25\pi$. Unlike the case with an opaque background, here it is found two dips in the transmission spectrum, caused by the contribution from the transparent background. Specifically, Eq. (9) shows that the final transmission contains three parts, which can be rewritten as $t = 1 + t_1 + t_2$, where $t_1 = 4\Gamma_0 \cos^2(\eta)/\left[\mathrm{i}(f - f_0 - \kappa) - 4\Gamma_0 \cos^2(\eta)\right]$ and $t_2 = 4\Gamma_0 \sin^2(\eta)/\left[\mathrm{i}(f - f_0 + \kappa) - 4\Gamma_0 \sin^2(\eta)\right]$ represent the scatterings from the two modes. Both t_1 and t_2 are equal to -1 (possessing a 180° phase) at their resonance frequencies (Fig. 4c). The presence of the background transmission (i.e., the first term in Eq. (9)) completely changes the EM responses of the whole system. The phase coverage is mainly contributed by two transmission bands at low and high frequencies (Fig. 4a, b), which is quite different from its opaque-background counterpart (Fig. 2a, b). Such difference can be better understood from the evolutions of Smith curves shown in Fig. 4d, where the interference between t_1 and t_2 first slightly merge two individual circles while adding the background transmission, and

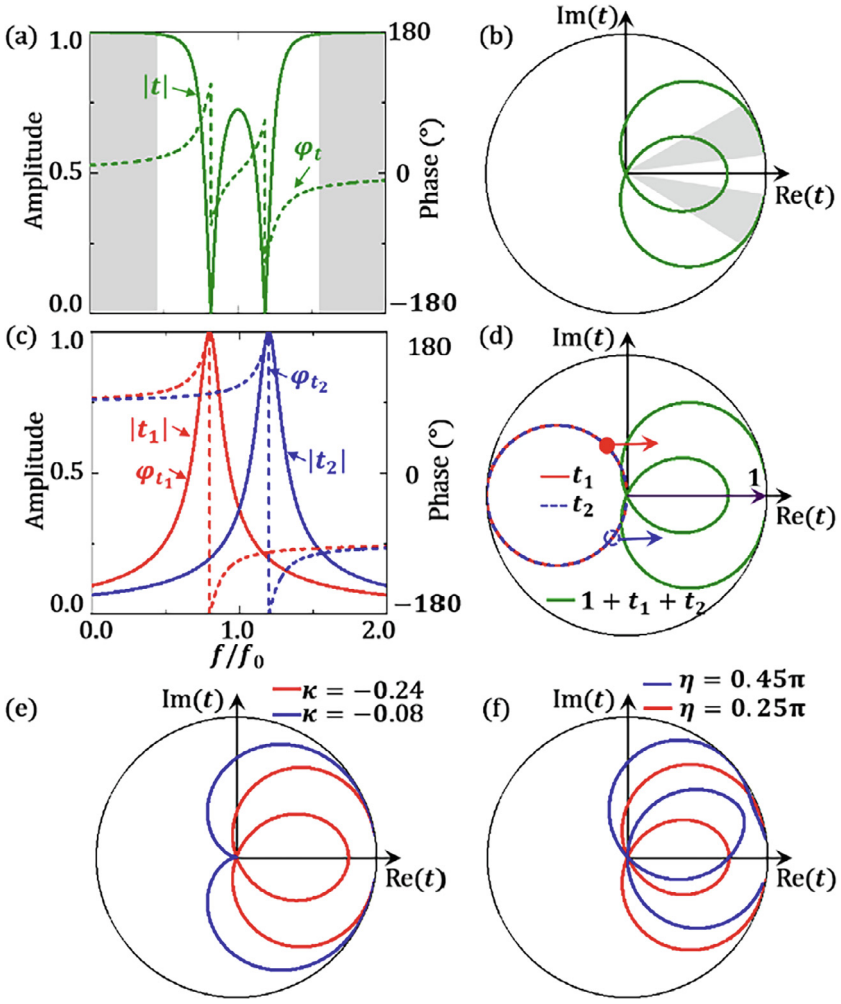

Fig. 4. Phase coverage for a 2-mode 2-port model in a transparent background. (a) CMT-computed spectra of transmission amplitude (solid line), phase (dashed line), and (b) Smith curves for a 2-mode 2-port model in a transparent background with parameters $\kappa/f_0 = -0.2, \Gamma_0/f_0 = 0.04$ and $\eta = 0.25\pi$. (c) Transmission amplitude (solid line), phase (dashed line), and (d) Smith curves of t_1 (red) and t_2 (blue) calculated by CMT with 2-port 2-mode (a transparent background) model. Smith curves of the transmission coefficient t with different CMT model (e) $\kappa/f_0 = -0.24, -0.08$ (red, blue), $\eta = 0.25\pi$, $\Gamma_0/f_0 = 0.04$, and (f) $\eta = 0.45\pi, 0.25\pi$ (red, blue), $\kappa/f_0 = -0.20$, $\Gamma_0/f_0 = 0.04$.

then shifts the whole curve from the left region to the right one. It is not surprising that the phase coverage is strongly dependent on the inter-mode coupling κ/Γ_0 (Fig. 4e), sharing the same physics as that discussed in the opaque-background model (Fig. 2). Moreover, there is a new degree of freedom in such a system, i.e., the phase difference η between two original resonators. It can be exploited to significantly modify the Smith curve, resulting in different phase coverage (Fig. 4f). Through adjustment of κ and η, the response of the system can be effectively changed, thus yielding phases covering different ranges. In particular, when the condition meets $\eta = \pi/4, \kappa = 0$, the transmission coefficient has a magnitude of 1 with the phase covering from 0 to 2π. Many applications have been implemented around the optical band on this basis [26,48]. However, such a condition $\eta = \pi/4$ and $\kappa = 0$ usually requires wavelength-scale 3D structures, which is not easy to be realized by metasurfaces with subwavelength thickness.

The above CMT analyses help us establish the following guidelines to build transmissive meta-devices with distinct functionalities. (1) Subwavelength multilayer meta-atoms with 2 or 3 layers with opaque background, no matter in an opaque background or a transparent one, can only provide phases covering particular ranges. Therefore, using such meta-atoms alone is not suitable for constructing wavefront-control meta-devices, but is acceptable in many polarization-control applications. (2) It is possible to adopt meta-atoms of the same type to build wavefront-control meta-devices, but the number of layers must be large enough, which is unfavorable for many application scenarios. (3) A more advisable approach is combining meta-atoms of different types, with phase coverage ranges compensating each other, so as to build wavefront-control devices requiring full-range phase coverage.

3. Practical meta-atom designs and application demonstrations

In this section, numerical simulations and microwave experiments are carried out to demonstrate three different meta-devices constructed by different types of multilayer meta-atoms, following the general design guidelines discussed in last section.

3.1. Quarter wave-plate

First how to use a 2-layer meta-atom to design a polarization-control meta-device is illustrated. The meta-atom is schematically depicted in Fig. 5a, consisting of a cross-shape resonator inserted in subwavelength-size metallic mesh, where each metallic layer is fabricated on a 0.5-mm-thick dielectric substrate ($\varepsilon_r = 2.95 + 0.005i$) and the inter-layer distance is denoted by h. Obviously, such a meta-atom can be described by the 2-port 2-mode model (Fig. 2b) studied in last section [49]. We first search

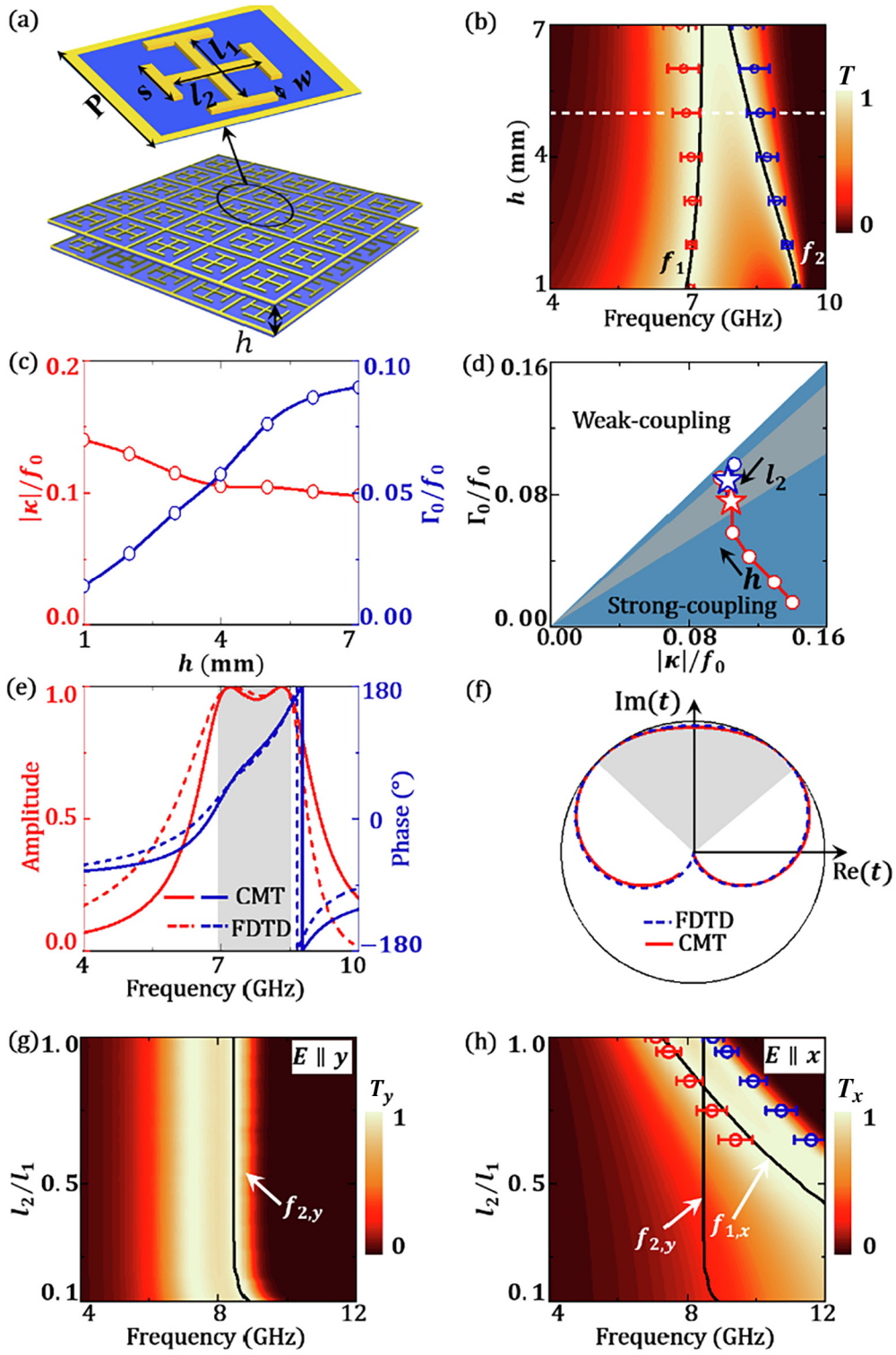

Fig. 5. Simulation results of the two-layer structure. (a) Schematics of the two-layer structure. (b) Transmittance spectra versus thickness h computed by FDTD simulations, where the solid black lines denote the perfect transmission peak, and the symbols (error-bars) denote the resonating frequencies (radiation damping rates) calculated with CMT. (c) CMT parameters κ, Γ_0 as a function of thickness h obtained by fitting FDTD-simulations. (d) $\kappa - \Gamma_0$ phase diagram, where the shaded area indicates the intermediate region and the red (blue) star symbols denote the designed meta-atoms for y-polarization (x-polarization). (e) Transmission amplitude (red) and phase (blue) spectra, and (f) Smith curves of two-layer system, where dashed lines denote simulated curves and solid lines denote CMT curves with $f_0 = 7.76$, $\kappa = -0.81$, $\Gamma_0 = 0.59$, all in units of GHz. (g) T_y and (h) T_x vary against bar length l_2, where the black lines represent the frequencies $f_{1,x}$ and $f_{2,y}$ for the 1st mode with x-polarization and the 2nd mode with y-polarization.

for meta-atoms with balanced κ and Γ_0 that can be used for our purpose. Fig. 5b depicts the FDTD-simulated spectra of a series of such structures with identical bar lengths ($l_1 = l_2 = 6$ mm) but different inter-layer distance h. Simulation results show that the EM properties of two transmission peaks, associated with symmetric and anti-symmetric modes of the model, can be dramatically controlled by the parameter h. All simulated spectra are well described by the 2-mode CMT model established in last section, with one particular example ($h = 5$ mm, corresponding to the dashed line in Fig. 5b) explicitly studied in Fig. 5e. Thus all model parameters

are successfully retrieved from the simulation results for realistic structures. Fig. 5c presents how the two model parameters ($|\kappa|/f_0$, Γ_0/f_0) vary against h. It is found $|\kappa| \ll f_0$, indicating a weak coupling between resonators in neighboring layers. To see how well the CMT analyses work, Fig. 5b depicts the positions of transmission peaks (symbols) and associated bandwidths (error bars), obtained by the CMT model with parameters shown in Fig. 5c. Comparisons show that the CMT model has indeed captured all essential features of the FDTD ones. The two CMT parameters have distinct dependences on h. Clearly, κ is a decreasing function of h, since the wave-function overlapping decreases as h increases. On the contrary, Γ_0 is an increasing function of h, caused by the decreased capability of a metallic mesh to block EM waves as h increases.

The intrinsic connection between h and the CMT parameters (Fig. 5c) motivates us to establish the following strategy to search for appropriate meta-atoms. Clearly, adjusting h can effectively control the two CMT parameters (κ and Γ_0), which in turn, drives the model moving in the phase diagram (see red open circles shown in Fig. 5d), finally arriving at an appropriate position (denoted as the red star) in the optimized region. Fig. 5e and f depict the simulated and CMT-calculated transmission spectra of the optimized structure (See Supplementary Information Section II for more fitting results), both exhibiting an optical transparency window (OTW) during $7.1 - 8.3$ GHz covering a phase variation range of around 90°.

After the basic structure with optimized h is found, how to design the quarter wave plate is discussed by further exploiting the lateral anisotropy of the structure. Obviously, it needs to adjust one of the length bars (say, l_2); while other geometric parameters (l_1 and h) are kept unchanged, in order to open enough cross-polarization phase difference at a given frequency. Fig. 5g and h depict how the transmission spectrum changes with the adjustment of l_2 for two different incident polarizations. The adjustment of l_2 is found to drastically change the x-polarized transmission spectra (Fig. 5h) but have little impact on the y-polarized spectra (Fig. 5g). Therefore, as l_2 takes a particular value (4.9 mm), the low-frequency peak in the x-polarized spectrum coincides well with the high-frequency peak in the y-polarized spectrum, yielding a 90° phase difference at this particular frequency yet with almost perfect transmittance for both polarizations, as illustrated in Fig. 5h. To better illustrate the physics, the CMT parameters are retrieved for the series of x-polarized spectra as shown in Fig. 5h (see Supplementary Information Section III for details), and then their positions are depicted as blue circles in the phase diagram (Fig. 5d). Interestingly, the adjustment of l_2 only drives the system to move inside the optimized region. In fact, while adjusting l_2 changes the resonant frequency (f_0) of the original mode and in turn changes both Γ_0 and κ associated with that mode, it does have significant impacts on the ratio of Γ_0/κ. As a result, the system still stays in the intermediate region. Thus, the lateral anisotropy is fully applied to finally reach a design, with two polarizations both located inside the intermediate region yet exhibiting large enough phase difference.

The quarter-wave plate is fabricated according to the design, with metallic structures printed on a 0.5-mm-thick F4B-PCB ($\epsilon_r = 2.95 + 0.005i$), separated by 5 mm – thick spacers made by polymethacrylimide (PMI, with $\epsilon_r = 1.02$) (see sample photo in Fig. 6a). In the measurements, the sample is shined normally with microwaves emitted from a horn antenna placed 1m away from the sample, and then another horn antenna placed 1 m away from the sample is used to collect the transmitted signals. Both source and receiver are connected to a vector-field analyzer (Agilent E8362c) so that both the amplitudes and phases of the transmitted signals can be obtained. Open symbols in Fig. 6b, c are the measured transmission spectra for the designed device under two

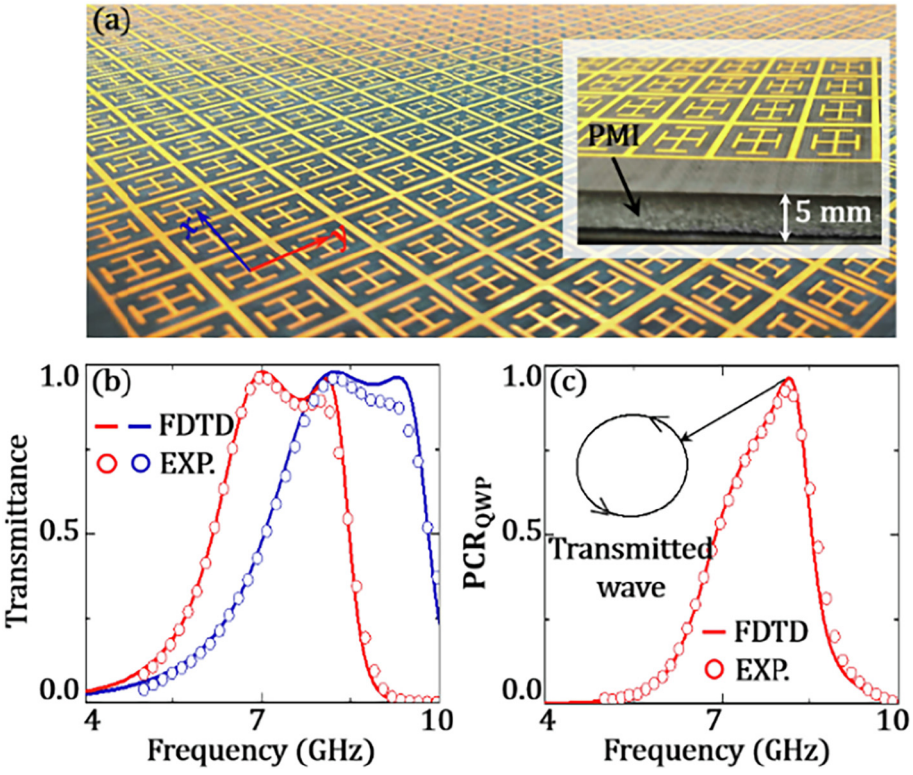

Fig. 6. Experimentally measured results for QWP. (a) Photograph of the experimental QWP sample, and the inset is a side view. (b) Experimental measured (symbols) and simulated (solid line) transmittance T_y (red) and T_x (blue) spectrum for two polarizations. (c) Experimental measured (symbols) and simulated (solid line) PCR_{QWP} spectrum.

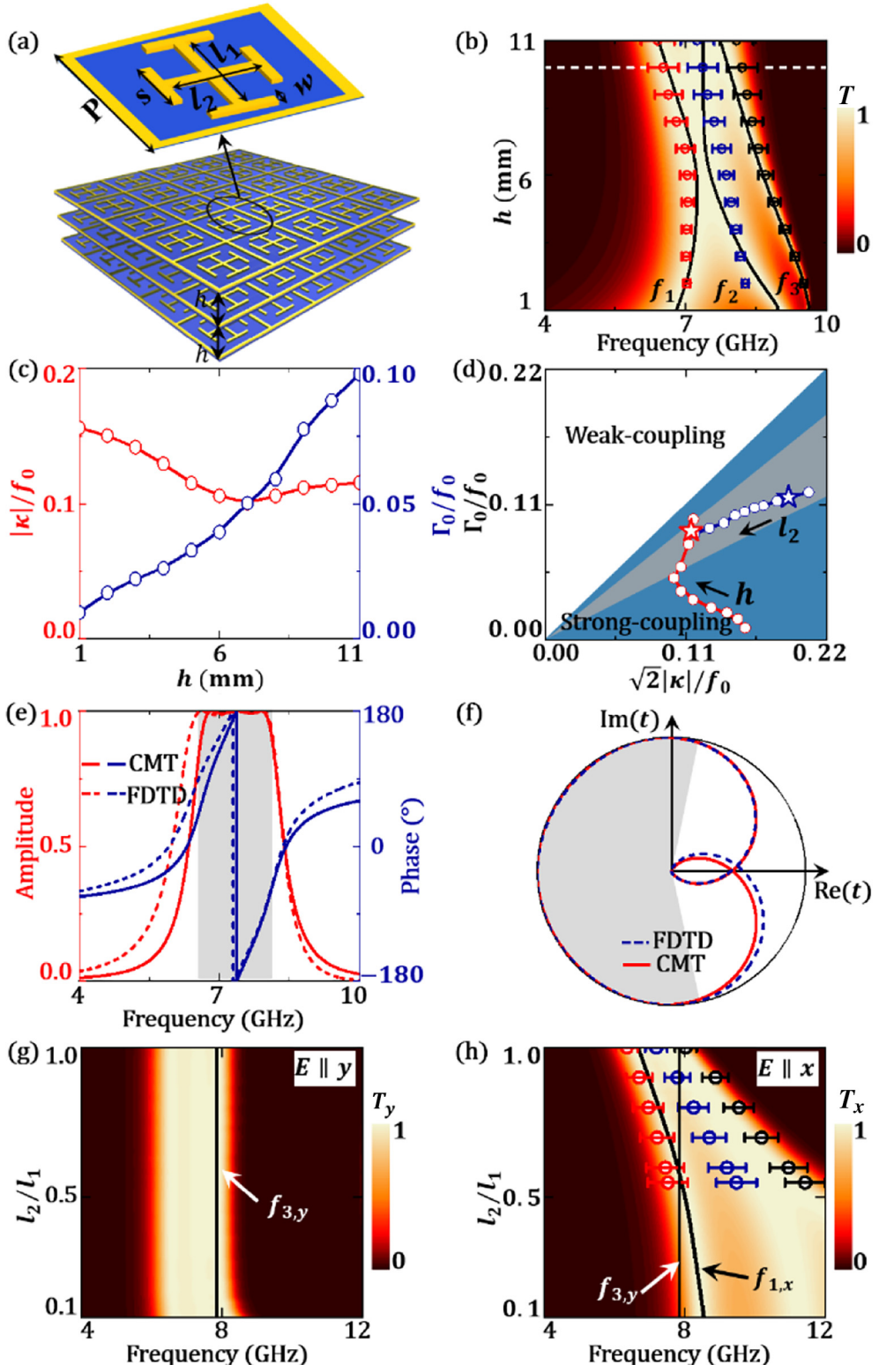

Fig. 7. Simulation results of the three-layer structure. (a) Schematics of the three-layer structure. (b) Transmittance spectra versus thickness h computed by FDTD simulations, where the solid black lines denote the perfect transmission peak, and the symbols (error-bars) denote the resonating frequencies (radiation damping rates) calculated with CMT. (c) CMT parameters κ, Γ_0 as a function of thickness h obtained by fitting FDTD-simulations. (d) $\kappa - \Gamma_0$ phase diagram, where the shaded area indicates the intermediate region and the red (blue) star symbols denote the designed meta-atoms for y-polarization (x-polarization). (e) Transmission amplitude (red) and phase (blue) spectra, and (f) Smith curves of three-layer system, where dashed lines denote simulated curves and solid lines denote CMT curves with $f_0 = 7.36, \kappa = -0.59, \Gamma_0 = 0.65$, all in units of GHz. (g) T_y and (h) T_x vary against bar length l_2, where the black lines represent the frequencies $f_{1,x}$ and $f_{3,y}$ for the 1st mode with x-polarization and the 3rd mode with y-polarization.

polarizations, which are in perfect agreement with FDTD simulations. Define polarization-conversion ration $\mathrm{PCR}_{\mathrm{QWP}} = -\mathrm{Im}(t_x^* t_y)$ as the absolute conversion efficiency from linear polarization to circular polarization. The fabricated sample exhibits the largest

PCR (95%) at 8.13 GHz, with a 0.5 GHz bandwidth, inside which PCR is greater than 85% (Fig. 6c).

3.2. Half wave-plate

As the second demonstration, a half wave plate is designed based on a similar strategy. Previous theoretical analyses show that the 3-mode system can yield 180° phase coverage; therefore the three-layer structure (Fig. 7a) is adopted to perform the design. The design strategy is essentially the same as that adopted in the design of the quarter wave-plate. Specifically, first, the appropriate spacer thickness h is found to drive the system to reach the optimized region shown in Fig. 3e, and then the lateral anisotropy is fully utilized to open enough phase difference for two cross polarizations.

Fig. 7b depicts how the FDTD-simulated transmission spectrum of the three-layer system varies against h, indicating the evolutions of three perfect transmission peaks associated with three collective modes defined in Eq. (6). Again, these simulated spectra can be well described by the 3-mode CMT model, with the best-fitted model parameters (κ, Γ_0) plotted in Fig. 7c as functions of h. The two CMT parameters, Γ_0 and κ, exhibit similar dependence on h as that in the two-layer case, sharing the same underlying physics. Therefore, adjusting h can efficiently change Γ_0 and κ, which in turn, drives the system to move in the phase diagram until reaching an optimized position (with $h = 10$ mm) represented by the red star in Fig. 7d. Indeed, the transmission spectrum of the optimized system ($h = 10$ mm) exhibits a flat OTW with a phase change of 180° (Fig. 7e), in good agreement with the CMT-computed spectra with $f_0 = 7.36$ GHz, $\kappa = -0.59$ GHz, $\Gamma_0 = 0.65$ GHz (see Supplementary Information Section II for more fitting results). Fig. 7f depicts the Smith curves of such a structure obtained by FDTD simulations and CMT calculations, in consistent with the generic CMT analyses presented in last section (Fig. 3b).

The second-step design is conducted by adjusting the bar length of l_2, while other parameters are kept unchanged. Again, adjusting l_2 can shift the x-polarized resonances rather than the y-polarized ones. Therefore, such a l_2 is chosen to make the first peak in x-polarization coincide with the third peak in y-polarization. Interestingly, such an optimization process essentially makes the system (in term of x-polarization response) move inside the intermediate region, thereby reaching at a design exhibiting the largest possible cross-polarization phase difference, as shown by the trajectory of retrieved CMT parameters (see Supplementary Information Section III for detailed parameters) as l_2 is adjusted (Fig. 7d). At $l_2 = 3.5$ mm, a phase difference with 180° can be opened with an almost perfect transmittance for two polarizations, as illustrated in Fig. 7h.

Next, a sample is fabricated, with geometric parameters as $l_1 = 6, l_2 = 3.5, P = 10, s = 4, w = 0.5, a = 9$, all in units of mm (Fig. 8a is a photograph of the sample), and a microwave experiment is performed to characterize its transmission property in the same way as in last sub-section. Symbols in Fig. 8b are the measured transmittance spectra, which are in excellent agreement with FDTD simulations. Symbols and solid lines in Fig. 8c depict the spectra of PCR_{HWP} calculated from the experimental and simulation data, respectively, where $PCR_{HWP} = |t_{xx} - t_{yy}|^2/4$ describes the polarization conversion efficiency. Perfect agreement between experimental and simulation results is noted. Fig. 8c shows that an HWP with $PCR_{HWP} = 95\%$ at 7.59 GHz is achieved, exhibiting a 0.5 GHz bandwidth with $PCR_{HWP} > 85\%$.

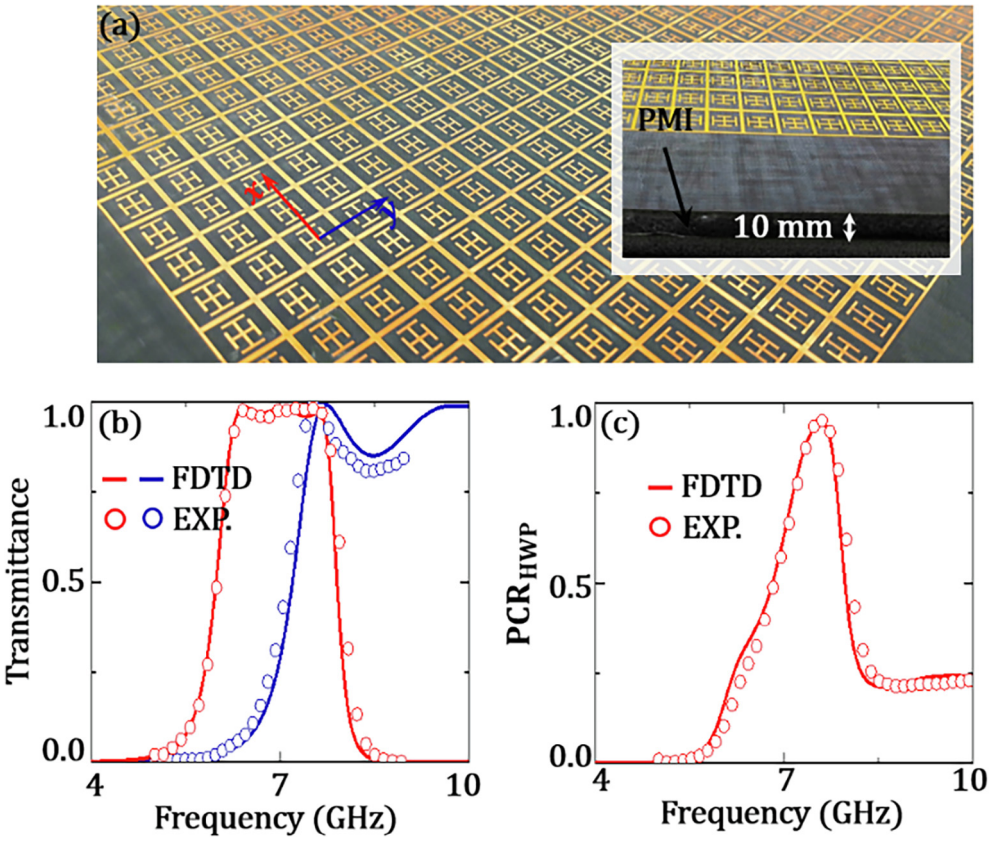

Fig. 8. Experimentally measured results for HWP. (a) Photograph of the experimental HWP sample, and inset is a side view. (b) Experimental measured (symbols) and simulated (solid line) transmittance T_y (red) and T_x (blue) spectrum for two polarizations. (c) Experimental measured (symbols) and simulated (solid line) PCR_{HWP} spectrum.

3.3. Beam deflector

Finally, how to design a beam deflector using multilayer meta-atoms with thin thickness is described for realizing high-efficiency anomalous refraction of EM waves. The construction of such a beam-deflection meta-device needs a series of meta-atoms, all allowing high transmissions of EM waves at the same frequency but exhibiting different transmission phases that are linearly varying in space covering the whole 360° region, as shown in Fig. 9b. Here, the working frequency of 8 GHz and the phase gradient of

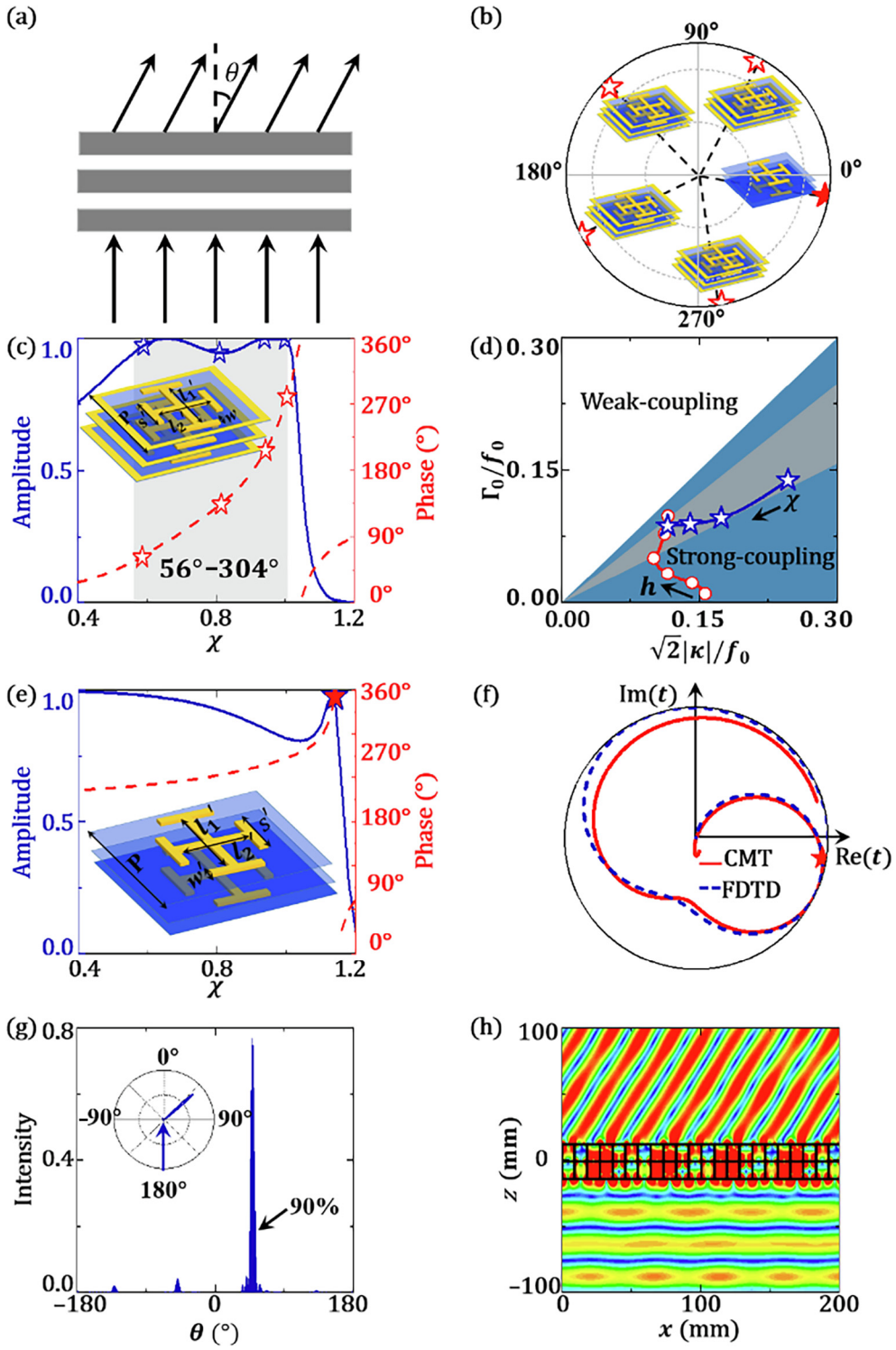

Fig. 9. Design of a beam deflector. (a) Schematic of a beam deflector meta-device. (b) Schematic of the phase distribution and transmission coefficient required by the beam deflector device. The open star symbols (solid star symbols) denote the transmission phase and amplitude of the opaque background three-layer model (the transparent background two-layer model). (c) Transmission amplitude (solid) and phase (dash) of the opaque background three-layer system as a function of scaling factor χ, where $l_1' = l_2' = \chi l_0, s' = \chi s_0$ ($l_0 = 6$ mm, $s_0 = 4$ mm). (d) $\kappa - \Gamma_0$ phase diagram, where the red (blue) symbols denote CMT parameters with varying thickness h (scaling factor χ). (e) Transmission amplitude (solid line) and phase (dashed line) of the transparent background two-layer system as a function of scaling factor χ. (f) Smith curves obtained by CMT (solid line) and FDTD (dashed line). (g) Far-field scattered intensity and (h) calculated electric field patterns at 8 GHz, where thin metallic sheets are inserted to separate two adjacent meta-atoms to reduce their mutual functional interferences.

$\xi = 0.75k_0$ are selected, so that the anomalous deflection angle is $\theta = \arcsin \xi/k_0 = 48.6°$. In addition, 5 meta-atoms are placed in one super cell; thus the phase difference between two adjacent meta-atoms is 72°, as illustrated in Fig. 9b.

How to achieve this goal based on meta-atoms with as few as possible layers is described here. Obviously, the meta-atoms with an identical type but more layers can be used to realize the desired phase coverage. However, the realized meta-device will be too thick. Alternatively, meta-atoms can be combined with different types, all possessing thin thicknesses but with phase coverage compensating each other. Since the phase coverage of the opaque-background 2-mode model (Fig. 1b) is too narrow (only 90°), the opaque-background 3-mode model (already providing 240° phase coverage) is selected as the major platform to design the meta-atoms. Through the similar design approach adopted in last two subsections, the interlayer distance h is optimized to drive the system into the intermediate region, and then the lateral structures are adjusted to find appropriate meta-atoms yielding desired transmission phases. According to the results of Fig. 7b, $h = 10$ mm is selected. As shown in Fig. 9c, the structural details of the metallic crosses in each layer are adjusted; while $h = 10$ mm, $w = 0.5$ mm, $P = 10$ mm are fixed in the first-step optimization. Then, meta-atoms with transmission phases inside the range of 56°–304° and with high transmittance ($T > 0.85$) at 8 GHz (shaded region in Fig. 9c) can be obtained. Such calculations facilitate to select four meta-atoms (see Supplementary Information Section IV for their geometrical parameters) yielding transmission phases 63°, 135°, 207°, 279°, correspondingly, as shown in Fig. 9b. Again, the roles of such two-step optimizations can be clearly seen from the two paths shown in the phase diagram (Fig. 9d): adjusting h effectively drives the system into the intermediate region (red symbols) while changing the lateral size of cross moves the system inside the intermediate region (blue symbols). However, a meta-atom with transmission phase 351° cannot be found based on such a searching strategy, due to the intrinsic limitation on phase coverage enabled by such a model (Fig. 9c). Therefore, it is necessary to find a meta-atom of another type providing the desired transmission phase that can never be covered by the adopted model. The generic discussions in Sec. 2 confirmed that the transparent-background models (Fig. 4b) can provide transmission phases compensating the opaque-background models (Fig. 3b). Thus, the transparent-background 2-mode model is taken as an additional platform to search for the desired meta-atom, with local resonator being a metallic cross without surrounding mesh (inset of Fig. 9e). Simple optimizations indicate that a meta-atom of this type with geometric parameters $P = 10,\ s = 4.572, l_1 = l_2 = 6.858,\ w = 0.5,\ h = 20$ (all in unit of mm) can yield a transmission phase 351°, meeting the requirement (Fig. 9b). Red line in Fig. 9f denotes the CMT-computed spectrum with model parameters $f_0 = 8.47$ GHz, $\kappa = -0.4$ GHz, $\Gamma_0 = 0.68$ GHz and $\eta = 0.53\pi$, in good agreement with the FDTD spectrum.

With all meta-atoms designed, then the meta-device is constructed with the super cell formed by these meta-atoms, and full-wave simulations are used to characterize its wave-manipulation properties. Fig. 9g shows that a pronounced light beam on transmission side occurs at the predicted deflection angle 48.6°, with an absolute efficiency of 90%. Here, the working efficiency is defined as the ratio between the power flow carried by the anomalously deflected beam (obtained by integration over the fill area shown by the arrow in Fig. 9g) and that of the incident beam. Fig. 9h presents the calculated electric-field patterns on the metasurface, which is shined by the normally incident EM wave at 8 GHz. Full-wave simulations clearly reveal how the deflected beam is generated and redirected to the anomalous angle with high efficiency.

As a short conclusion of this section, three meta-devices with different numbers of layers are demonstrated. However, these three meta-devices are designed with narrow bandwidths, since the target is the meta-devices with the lowest thicknesses and least number of layers. This issue is not an inherent limitation of our design method, which can be easily extended to design broadband wave-manipulation devices. For illustration, a broadband quarter-wave plate with a bandwidth of 1.2 GHz and working frequency around 7 GHz ($PCR_{QWP} > 85\%$) is designed by using three-layer structures instead of two-layer structures (see Supplementary Information Section V). Here, the key idea is to employ more layers to construct an optically transparent window with a larger phase-variation range, so that there is more flexibility in designing appropriate meta-devices with broadband performances. To further illustrate the powerfulness of our theory, the CMT model is also employed to study meta-devices with different resonators in each layer (see Supplementary InformationSection VI).

4. Conclusions

In summary, based on thorough CMT analyses, a generic phase diagram is established to understand the subtle interplays between phase coverage and thickness for multilayer meta-atoms belonging to different types, which have been widely used in building transmissive meta-devices. The inherent physics underlying such contradictions between phase coverage and thickness help establish a set of guidelines to facilitate the design of high-performance ultra-thin meta-devices for different purposes. For proving the concept, the guidelines are followed to design two polarization-control meta-devices (an HWP and a QWP) and a beam deflector, all working in transmission mode and with ultra-thin thicknesses; and microwave experiments and/or simulations are carried out to demonstrate their high performances. Our analyses can not only help people understand the intrinsic physics in such transmission meta-atom designs, but also guide people to realize high-efficiency transmissive metasurfaces for diversified practical applications.

Conflict of interest

The authors declare that they have no conflict of interest.

Acknowledgments

This work was supported by National Key Research and Development Program of China (2017YFA0303500) and the National Natural Science Foundation of China (11704240, 11734007, and 11674068), Natural Science Foundation of Shanghai (17ZR1409500 and 18QA1401800), Shanghai Science and Technology Committee (16JC1403100), Shanghai East Scholar Plan, and Fudan University-CIOMP Joint Fund.

Author contributions

Shiyi Xiao and Lei Zhou contributed to the conception of the research. Bowen Yang performed theoretical analyses, simulation and wrote the manuscript. Tong Liu helped theoretical analyses and wrote the manuscript. Huijie Guo performed the experimental measurement. All authors discussed the results and reviewed the manuscript.

Appendix A. Supplementary data

Supplementary data to this article can be found online at https://doi.org/10.1016/j.scib.2019.05.028.

References

[1] Yu NF, Capasso F. Flat optics with designer metasurfaces. Nat Mater 2014;13:139–50.
[2] Chen HT, Taylor AJ, Yu NF. A review of metasurfaces: physics and applications. Rep Prog Phys 2016;79:076401.
[3] Xiao SY, Wang JR, Liu F, et al. Spin-dependent optics with metasurfaces. Nanophotonics 2017;6:215–34.
[4] He Q, Sun SL, Xiao SY, et al. High-efficiency metasurfaces: principles, realizations, and applications. Adv Opt Mater 2018;6:1800415.
[5] Yu NF, Genevet P, Kats MA, et al. Light propagation with phase discontinuities: generalized laws of reflection and refraction. Science 2011;334:333–7.
[6] Ni XJ, Emani NK, Kildishev AV, et al. Broadband light bending with plasmonic nanoantennas. Science 2012;335:427.
[7] Aieta F, Genevet P, Yu NF, et al. Out-of-plane reflection and refraction of light by anisotropic optical antenna metasurfaces with phase discontinuities. Nano Lett 2012;12:1702–6.
[8] Sun SL, He Q, Xiao SY, et al. Gradient-index meta-surfaces as a bridge linking propagating waves and surface waves. Nat Mater 2012;11:426–31.
[9] Yin XB, Ye ZL, Rho J, et al. Photonic spin hall effect at metasurfaces. Science 2013;339:1405–7.
[10] Xiao SY, Zhong F, Liu H, et al. Flexible coherent control of plasmonic spin-hall effect. Nat Commun 2015;6:8360.
[11] Aieta F, Genevet P, Kats MA, et al. Aberration-free ultrathin flat lenses and axicons at telecom wavelengths based on plasmonic metasurfaces. Nano Lett 2012;12:4932–6.
[12] Li X, Xiao SY, Cai BG, et al. Flat metasurfaces to focus electromagnetic waves in reflection geometry. Opt Lett 2012;37:4940–2.
[13] Khorasaninejad M, Zhuit AY, Roques-Carmes C, et al. Polarization-insensitive metalenses at visible wavelengths. Nano Lett 2016;16:7229–34.
[14] Chen BH, Wu PC, Su VC, et al. Gan metalens for pixel-level full-color routing at visible light. Nano Lett 2017;17:6345–52.
[15] Hao JM, Yuan Y, Ran LX, et al. Manipulating electromagnetic wave polarizations by anisotropic metamaterials. Phys Rev Lett 2007;99:063908.
[16] Luo WJ, Xiao SY, He Q, et al. Photonic spin hall effect with nearly 100% efficiency. Adv Opt Mater 2015;3:1102–8.
[17] Pfeiffer C, Grbic A. Metamaterial huygens' surfaces: tailoring wave fronts with reflectionless sheets. Phys Rev Lett 2013;110:197401.
[18] Monticone F, Estakhri NM, Alu A. Full control of nanoscale optical transmission with a composite metascreen. Phys Rev Lett 2013;110:203903.
[19] Pfeiffer C, Emani NK, Shaltout AM, et al. Efficient light bending with isotropic metamaterial huygens' surfaces. Nano Lett 2014;14:2491–7.
[20] Sun SL, Yang KY, Wang CM, et al. High-efficiency broadband anomalous reflection by gradient meta-surfaces. Nano Lett 2012;12:6223–9.
[21] Pors A, Nielsen MG, Eriksen RL, et al. Broadband focusing flat mirrors based on plasmonic gradient metasurfaces. Nano Lett 2013;13:829–34.
[22] Xu HX, Liu HW, Ling XH, et al. Broadband vortex beam generation using multimode pancharatnam-berry metasurface. IEEE Trans Antennas Propag 2017;65:7378–82.
[23] Xu HX, Ma SJ, Ling XH, et al. Deterministic approach to achieve broadband polarization independent diffusive scatterings based on metasurfaces. ACS Photonics 2018;5:1691–702.
[24] Xu HX, Hu GW, Li Y, et al. Interference-assisted kaleidoscopic meta-plexer for arbitrary spin-wavefront manipulation. Light Sci Appl 2019;8:3.
[25] Ding XM, Monticone F, Zhang K, et al. Ultrathin pancharatnam-berry metasurface with maximal cross-polarization efficiency. Adv Mater 2015;27:1195–200.
[26] Decker M, Staude I, Falkner M, et al. High-efficiency dielectric huygens' surfaces. Adv Opt Mater 2015;3:813–20.
[27] Chen K, Feng YJ, Monticone F, et al. A reconfigurable active huygens' metalens. Adv Mater 2017;29:1606422.
[28] Xu HX, Hu GW, Han L, et al. Chirality-assisted high-efficiency metasurfaces with independent control of phase, amplitude, and polarization. Adv Opt Mater 2019;7:1801479.
[29] Chen S, Zhang Y, Li Z, et al. Empowered layer effects and prominent properties in few-layer metasurfaces. Adv Opt Mater, doi: 10.1002/adom.201801477.
[30] Cheng H, Liu ZC, Chen SQ, et al. Emergent functionality and controllability in few-layer metasurfaces. Adv Mater 2015;27:5410–21.
[31] Xu HX, Tang SW, Wang GM, et al. Multifunctional microstrip array combining a linear polarizer and focusing metasurface. IEEE Trans Antennas Propag 2016;64:3676–82.
[32] Sun WJ, He Q, Sun SL, et al. High-efficiency surface plasmon meta-couplers: concept and microwave-regime realizations. Light Sci Appl 2016;5:e16003.
[33] Li Z, Liu W, Cheng H, et al. Simultaneous generation of high-efficiency broadband asymmetric anomalous refraction and reflection waves with few-layer anisotropic metasurface. Sci Rep 2016;6:35485.
[34] Luo WJ, Sun SL, Xu HX, et al. Transmissive ultrathin pancharatnam-berry metasurfaces with nearly 100% efficiency. Phys Rev Appl 2017;7:044033.
[35] Wang Z, Dong SH, Luo WJ, et al. High-efficiency generation of bessel beams with transmissive metasurfaces. Appl Phys Lett 2018;112:191901.
[36] Pfeiffer C, Grbic A. Cascaded metasurfaces for complete phase and polarization control. Appl Phys Lett 2013;102:231116.
[37] Abdelrahman AH, Elsherbeni AZ, Yang F. Transmission phase limit of multilayer frequency-selective surfaces for transmitarray designs. IEEE Trans Antennas Propag 2014;62:690–7.
[38] Sun WJ, He Q, Hao JM, et al. A transparent metamaterial to manipulate electromagnetic wave polarizations. Opt Lett 2011;36:927–9.
[39] Grady NK, Heyes JE, Chowdhury DR, et al. Terahertz metamaterials for linear polarization conversion and anomalous refraction. Science 2013;340:1304–7.
[40] Mutlu M, Akosman AE, Serebryannikov AE, et al. Diodelike asymmetric transmission of linearly polarized waves using magnetoelectric coupling and electromagnetic wave tunneling. Phys Rev Lett 2012;108:213905.
[41] Mutlu M, Ozbay E. A transparent 90 degrees polarization rotator by combining chirality and electromagnetic wave tunneling. Appl Phys Lett 2012;100:051909.
[42] Xi B, Xu H, Xiao SY, et al. Theory of coupling in dispersive photonic systems. Phys Rev B 2011;83:165115.
[43] Hsu CW, DeLacy BG, Johnson SG, et al. Theoretical criteria for scattering dark states in nanostructured particles. Nano Lett 2014;14:2783–8.
[44] Xu H, He Q, Xiao SY, et al. Tight-binding analysis of coupling effects in metamaterials. J Appl Phys 2011;109:023103.
[45] Fan SH, Suh W, Joannopoulos JD. Temporal coupled-mode theory for the fano resonance in optical resonators. J Opt Soc Am A 2003;20:569–72.
[46] Wen DD, Chen SM, Yue FY, et al. Metasurface device with helicity-dependent functionality. Adv Opt Mater 2016;4:321–7.
[47] Cai T, Wang GM, Tang SW, et al. High-efficiency and full-space manipulation of electromagnetic wave fronts with metasurfaces. Phys Rev Appl 2017;8:034033.
[48] Yu YF, Zhu AY, Paniagua-Dominguez R, et al. High-transmission dielectric metasurface with 2 phase control at visible wavelengths. Laser Photon Rev 2015;9:412–8.
[49] Zhou L, Wen WJ, Chan CT, et al. Electromagnetic-wave tunneling through negative-permittivity media with high magnetic fields. Phys Rev Lett 2005;94:243905.

Bowen Yang is currently pursuing a Master degree at School of Communications and Information Engineering, Shanghai University. He received his B.Eng. degree in Electronic and Information Engineering from North China University of Water Resources and Electric Power in 2017. His work focuses on electromagnetic metasurface.

Shiyi Xiao received his Ph.D. degree from the Physics Department, Fudan University in 2013, and then worked as a research fellow in the School of Physics and Astronomy at University of Birmingham from 2014 to 2016. He is currently a professor in the School of Communications and Information Engineering, Shanghai University. His research interests cover metamaterials, nanophotonics, and plasmonics.

Lei Zhou received his Ph.D. degree in Physics from Fudan University, China, in 1997. From 1997 to 2000, he was a postdoctoral fellow of Institute for Material Research in Tohoku University. He joined Physics Department of Fudan University in 2004 as a professor, and became a "Xi-De" chair professor in 2013. His research interests cover magnetism, metamaterials, photonic crystals, and plasmonics.